Chemical Engineering Journal 532 (2026) 174177

Contents lists available at ScienceDirect

Chemical Engineering Journal

journal homepage: www.elsevier.com/locate/cej

Dual-stimuli magnetic drug nanoparticles for chemoimmunotherapy: Magnetically driven, charge-reversal enhanced tumour penetration and pH-triggered drug release

Xue Feng [a,1], Hongdi Wang [a,b,c,1], Yuxiang Xue [a], Nurbanu Ozgultekin [a], Takanori Kitamura [b], Jin Li [c], Defang Ouyang [d], Guangyu Zhu [e], Guangzhao Mao [a], Bin-Zhi Qian [b,f,*], Xianfeng Chen [a,**]

[a] School of Engineering, Institute for Bioengineering, University of Edinburgh, The King's Buildings, Edinburgh, EH9 3JL, UK
[b] Centre for Reproductive Health, College of Medicine and Veterinary Medicine, Queen's Medical Research Institute, The University of Edinburgh, Edinburgh, UK
[c] Cardiff School of Engineering, Cardiff University, Cardiff, CF24 3AA, UK
[d] State Key Laboratory of Quality Research in Chinese Medicine, Institute of Chinese Medical Sciences (ICMS), University of Macau, 999078, Macao
[e] Department of Chemistry, City University of Hong Kong, 83 Tat Chee Ave, Kowloon Tong, Hong Kong
[f] Fudan University Shanghai Cancer Center, Department of Oncology, Shanghai Medical College, The Human Phenome Institute, Zhangjiang-Fudan International Innovation Center, Fudan University, Shanghai, 200433, China

ARTICLE INFO

Keywords:
Magnetic nanomedicine
Chemo-immunotherapy
Deep tumour penetration
Carrier-free drug nanoparticles
Magnetic field–guided delivery
High drug loading
Tumour immune microenvironment

ABSTRACT

Poor intratumoral penetration remains a major obstacle to effective chemotherapy, caused by dense extracellular matrices, high interstitial pressure, and abnormal vasculature. Magnetic nanoparticle (NP)-mediated drug delivery provides spatial control, but existing systems suffer from low drug loading, weak responsiveness to tumour microenvironments, and limited penetration. Here, we report for the first time a self-assembled nanoplatform in which ultrasmall Fe_3O_4 NPs are evenly distributed within a carrier-free doxorubicin (DOX) core and surface-modified with glycol chitosan (Fe_3O_4-DOX@GC NPs). This unique architecture simultaneously achieves ultra-high drug loading (69%) and markedly enhances responsiveness to external magnetic fields, addressing two long-standing challenges in magnetic nanomedicine. In addition, tumour acidity triggers a surface charge reversal from negative to positive, promoting efficient cellular uptake. In 3D tumour spheroids, dual static and alternating magnetic fields increased DOX retention by 2.02-fold compared with static fields alone. In vivo, magnetic guidance produced a 6.3-fold increase in tumour accumulation and a 58% tumour volume reduction relative to free DOX. Importantly, the nanoplatform also activated antitumour immunity, significantly expanding cytotoxic T cells and antitumoral macrophages. This first-in-class dual chemotherapeutic–immunotherapeutic nanoplatform establishes a powerful strategy to overcome tumour penetration barriers while reshaping the immune microenvironment for improved cancer therapy.

1. Introduction

Nanomedicines are drug-loaded nanoparticles (NPs) that offer several advantages over conventional medicines, including enhanced solubility, improved pharmacokinetics, targeted delivery, and reduced systemic toxicity [1,2]. Yet, their clinical translation is often limited by the complex architecture of solid tumours, characterised by abnormal vasculature, dense extracellular matrix, heterogeneous stromal cells, and elevated interstitial fluid pressure. These features restrict nanoparticle penetration and efficacy [3–6].

PEGylation is widely used to improve nanomedicine stability and circulation time, enabling passive tumour targeting in preclinical and clinical settings [7,8]. However, their neutral or slightly negative surface charge limits uptake by negatively charged tumour cells. For

* Correspondence to: B.-Z. Qian, Centre for Reproductive Health, College of Medicine and Veterinary Medicine, Queen's Medical Research Institute, The University of Edinburgh, Edinburgh, UK.
** Corresponding author.
E-mail addresses: Binzhi.Qian@ed.ac.uk (B.-Z. Qian), Michael.Chen@ed.ac.uk (X. Chen).
[1] These authors contributed equally.

https://doi.org/10.1016/j.cej.2026.174177
Received 28 August 2025; Received in revised form 6 January 2026; Accepted 13 February 2026
Available online 18 February 2026

example, Doxil (an FDA-approved formulation) penetrates only ~18.8 μm into mouse tumours [9,10]. While positively charged particles promote ATP-dependent uptake, they are prone to rapid clearance from the bloodstream [11,12]. Charge-reversal coatings address this trade-off by maintaining stability in circulation and switching to a positive charge at the tumour site [13–15].

Nonetheless, tuning nanomedicine's physicochemical properties alone has proven insufficient for deep tumour penetration. External forces, such as magnetic manipulations, have been explored to actively drive nanomedicine into tumour tissues [16]. Co-assembly offers an efficient approach to integrate drugs and magnetic nanoparticles (MNPs) into a single nanoplatform for magnetically assisted drug delivery. In most existing studies, auxiliary matrix materials—such as poly (lactic-*co*-glycolic acid) (PLGA), engineered polymers, or proteins—are used to entrap both components [17–19]. While effective, these carrier-based systems often require multi-step synthesis, dilute the drug phase, and spatially segregate magnetic nanoparticles from the therapeutic payload, thereby limiting both drug loading and magnetic responsiveness.

To address these limitations, direct co-assembly of active constituents has emerged as a promising strategy to simultaneously achieve high drug loading and multifunctionality. Representative examples include electrostatic co-assembly of citric acid-functionalised Fe_3O_4 nanoparticles with doxorubicin [20], host–guest-driven co-assembly of β-cyclodextrin-decorated Fe_3O_4 nanoparticles with polymerised paclitaxel [21], and related polymer- or protein-assisted magnetic drug delivery systems [22–25]. However, these approaches still rely on auxiliary scaffolds or matrices that separate drug and magnetic components and preclude the formation of a fully integrated, carrier-free drug architecture.

Here, we report a rapid, one-step co-assembly strategy that produces a distinct class of magnetic drug nanomedicine: a carrier-free drug nanoparticle in which ultrasmall Fe_3O_4 nanoparticles (~10 nm) are homogeneously embedded throughout the interior of the drug matrix itself. Through direct co-assembly of hydrophobic doxorubicin (DOX) with oleic acid-coated Fe_3O_4 nanoparticles, we obtain a structurally integrated nanomedicine composed exclusively of active constituents. This unique internal organisation enables the simultaneous realisation of ultra-high drug loading (69%) and high MNP density (each construct contains >6800 Fe_3O_4 particles), resulting in enhanced magnetic field responsiveness and emergent immunomodulatory effects that are not accessible in conventional carrier-mediated or surface-loaded magnetic drug systems. This is achieved through an optimised precipitation process that ensures their uniform spatial distribution within the drug matrix. Subsequent coating with DSPE-PEG-COOH provides reactive sites for conjugation with glycol chitosan (GC), enabling pH-responsive charge reversal [26,27]. In the mildly acidic tumour microenvironment, Fe_3O_4-DOX@GC NPs convert from negative to positive [28], enhancing cellular uptake and retention (Scheme 1). The high magnetic content further amplifies penetration under external fields, boosting both propulsion and targeted DOX delivery. Beyond chemotherapy, these NPs modulate the tumour immune microenvironment in vivo, improving therapeutic outcomes in mouse tumour models. Through the integration of high drug payload, evenly distributed magnetic cores, magnetic actuation, and pH-triggered charge reversal, our Fe_3O_4-DOX@GC NPs overcome the long-standing barriers of extravasation, deep penetration, and efficient cellular internalisation, representing a significant advance in nanomedicine design for cancer therapy.

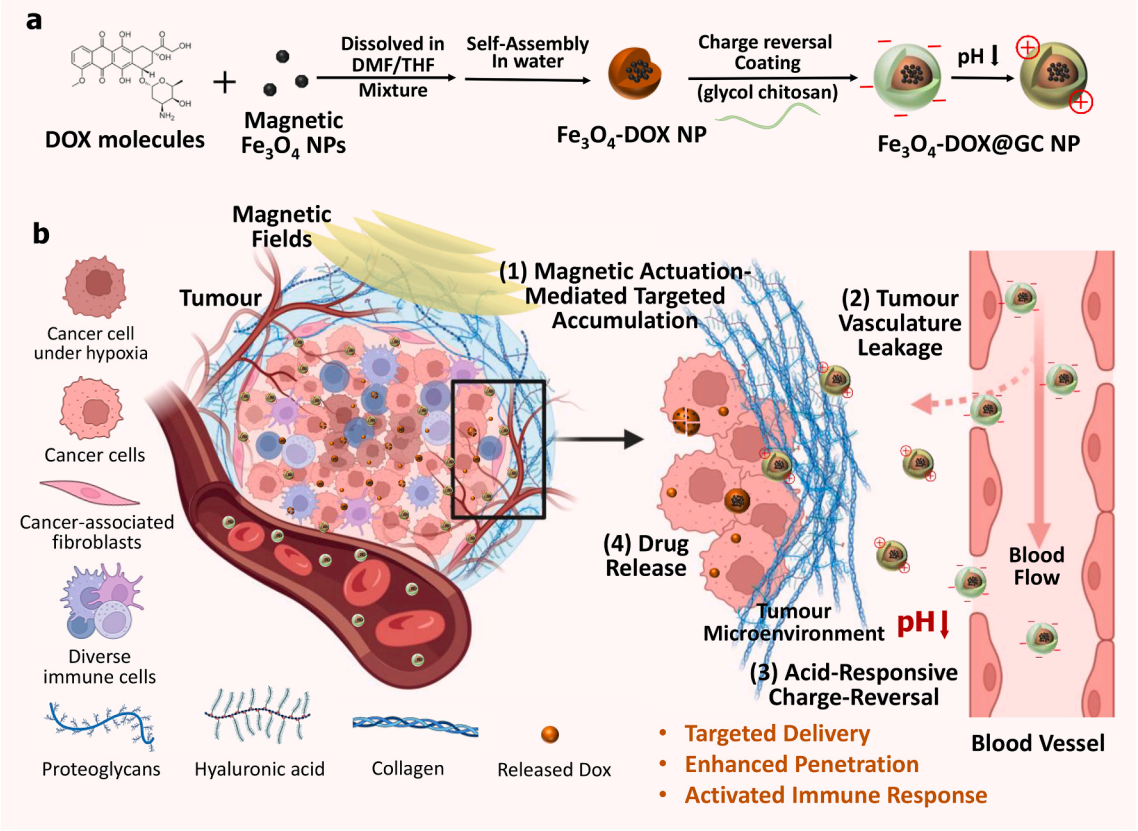

Scheme 1. a. Schematic representation illustrating the fabrication of GC-coated, self-assembled magnetic DOX NPs, which undergo a surface charge transition from negative to positive in an acidic environment. b. Diagram showing the application of GC-coated magnetic DOX NPs for magnetic targeting and deep penetration into mouse tumour tissues. Magnetic fields actively direct these charge-reversal NPs to accumulate at the tumour site, thereby overcoming multiple biological barriers and facilitating the delivery of anticancer drugs deep within the tumour while simultaneously reprograming the tumour immune microenvironment.

2. Methods

2.1. Materials

Iron(III) chloride hexahydrate ($FeCl_3{\cdot}6H_2O$), oleic acid (OA) (90%), 1-octadecene, sodium oleate, hexane, triethylamine (TEA), 1-Ethyl-3-(3-dimethylaminopropyl)carbodiimide (EDC), N-Hydroxysuccinimide (NHS), Glycol chitosan (GC) (≥ 60%, titration), meso-2,3-Dimercaptosuccinic acid (DMSA), N, *N*-dimethylformamide anhydrous 99.8% (DMF), and tetrahydrofuran anhydrous 99.9% (THF) were purchased from Sigma-Aldrich. Doxorubicin hydrochloride was obtained from Stratech. DSPE-PEG-COOH (MW 5 K) was bought from Creative PEGWorks. L-Lactic acid (anhydrous, 98%) was from Thermo Scientific.

2.2. Preparation of OA-Fe_3O_4 NPs

Ultra-small OA-Fe_3O_4 NPs were synthesised by using Park's method with adaption [29].

2.3. Synthesis of Fe_3O_4-DOX NPs and pure DOX NPs

Fe_3O_4-DOX NPs were synthesised via a solvent exchange method. Briefly, 10 mg of doxorubicin hydrochloride (DOX·HCl) was dissolved in 10 mL of DMF (1 mg/mL) with 10 μL of TEA and stirred overnight at room temperature to convert hydrophilic DOX·HCl to its hydrophobic form. The hydrophobic DOX was then mixed with OA-Fe_3O_4 NPs at varying weight ratios in a mix solvent of DMF and THF at volume ratio of 10: 1. The organic mixture was transferred into a syringe with a needle and added dropwise to deionised (DI) water under vigorous magnetic stirring. The addition rate was precisely controlled using a syringe pump (NE-1000) set to a flow rate of 2 mL/min. After 10 min, DSPE-PEG-COOH (2 mg/mL), an amount equal to the total mass of DOX and OA-Fe_3O_4 was added. This was followed by 5 min of stirring and 15 min of sonication. The resulting Fe_3O_4-DOX NPs, functionalised with –COOH groups, were purified using 10 kDa Amicon® Ultra Centrifugal Filters at 4 °C to remove organic solvents and free drugs.

Pure DOX NPs were synthesised by the same procedure as Fe_3O_4-DOX NPs except the DOX was dissolved in THF solvent and then added dropwise to DI water.

2.4. Surface functionalisation of Fe_3O_4-DOX NPs with GC

Fe_3O_4-DOX NPs were further functionalised with GC via an amidation reaction. Briefly, 2 mg of DSPE-PEG-COOH-coated Fe_3O_4-DOX NPs were dissolved in 6 mL of Phosphate Buffer Saline (PBS, pH 6.0), followed by the addition of 2 mg of EDC and 6 mg of NHS. After 15 min of stirring, 10 mg of GC was added, and the pH was adjusted to 8.0 with 1 M NaOH. The reaction proceeded for 12 h at room temperature, after which the GC-coated NPs were washed three times with ultrapure water and stored at 4 °C.

2.5. Characterisation of synthesised NPs

The morphology and size of synthesised NPs were characterised by transmission electronic microscopy (TEM, JEOL TEM-1400). The particle size was measured using ImageJ software ($n > 30$), and the data obtained were analysed as the mean ± standard deviation. The Zeta potential and hydrodynamic size of NPs were determined by a Malvern dynamic laser scattering instrument (DLS, Zetasizer Nano ZS 90, Malvern, UK) at 25 °C ($n = 3$). The UV–Vis spectrum of NPs was measured by a Nanodrop spectrophotometer (Nanodrop 2000c, ThermoFisher™ Scientific).

The magnetic property of OA-Fe_3O_4 NPs was measured with the vibrating sample magnetometer (VSM, Quantum Design PPMS® DynaCool™ measurement system) at 300 K.

To determine the drug encapsulation efficiency (DEE), the Fe_3O_4-DOX NPs were dissolved in DMSO to break NPs and the emission of DOX was analysed by a microplate reader (CLARIOstar® plus). A standard curve of DOX/DMSO solution with different DOX concentrations was obtained, with the excitation at 480 nm and emission at 595 nm. The DEE of DOX was calculated according to the following formula:

$$\text{DEE}\ (\%) = \frac{\text{The weight of DOX in NPs}}{\text{The weight of DOX added in preparation}} * 100\% \quad (1)$$

To determine the loading efficiencies (LE) of DOX and Fe_3O_4 in the Fe_3O_4-DOX@GC NPs, the amount of loaded DOX was quantified using the same method as employed in the DEE analysis. The Fe_3O_4 NP content was measured using inductively coupled plasma optical emission spectroscopy (ICP-OES, Perkin Elmer Optima 5300 DV ICP-OES). Specially, 40 μL of Fe_3O_4-DOX@GC NP suspension was pipetted into a glass vial, followed by the addition of 1.071 mL of 70% nitric acid to digest the iron oxide. The samples were digested for 48 h. Then, the solution was diluted with DI water to a final volume of 15 mL for Fe concentration measurement in ICP-OES. A series of standard solutions of Fe/nitric acid (5%) were also prepared by diluting the commercial Fe standard solution (Sigma, 1000 mg/L) for ICP-OES analysis. Finally, the LE of DOX or Fe_3O_4 within the NPs was calculated using the following equation:

$$\text{LE}\ (\%) = \frac{\text{The weight of DOX or Fe3O4 in NPs}}{\text{The total weight of NPs}} * 100\% \quad (2)$$

2.6. Drug release of NPs in vitro

DOX release from Fe_3O_4-DOX@GC NPs was evaluated using a dialysis method in PBS buffers at pH 7.4, 6.5, and 5.0, and DMEM medium (without phenol red) containing 10% FBS. NPs (0.2 mg/mL DOX) were placed in a 3500 Da dialysis bag and immersed in 25 mL of release buffer at 37 °C with shaking (180 rpm). At specified intervals, 2 mL of release medium was collected for UV–Vis analysis (OD at 480 nm), and fresh buffer was replenished. Standard curves of DOX/PBS at different pH values were used for quantification (Fig. S12).

2.7. Cell culture

MDA-MB-231, MCF-7 (human breast adenocarcinoma cancer cells), 4T1 (mouse mammary breast cancer cells), and HUVECs (Human Umbilical Vein Endothelial Cells) cell lines were bought from ATCC®. Cells were maintained in DMEM medium containing 10% FBS, 1% penicillin G and 1% streptomycin and incubated at 37 °C in a humidified 5% CO_2 atmosphere.

2.8. Cell viability assay

The cytotoxicity of NPs at different pH values was assessed by the MTT cell viability assay according to the manufacturer's suggested procedures. Briefly, 1×10^4/well MDA-MB-231 cells were seeded into 96-well plates in 200 μL of the growth medium, and incubated for 24 h at 37 °C/5% CO_2. Then, the old medium in each well was replaced with 150 μL of no FBS fresh medium (pH 7.4 & 6.8) containing NPs at DOX concentrations of 1, 5, and 10 μg/mL. The pH value of the culture medium was adjusted by lactate. After incubating for 48 h, the cells were carefully washed with the fresh medium, and 100 μL of original DMEM medium was added to each well. Next, 15 μL of MTT (5 mg/mL) was added to each well and incubated for 4 h at 37 °C. The medium in each well was aspirated, and 150 μL of DMSO was added to dissolve the formed formazan. The plate was read at 570 nm (O.D.) using a plate reader (CLARIOstar® plus) and the cell viability was calculated. The data are expressed as mean values ± standard deviation of three measurements.

The cytotoxicity of NPs on different cell lines (4T1 and HUVECs) with normal cell culture medium (pH 7.4) was also evaluated by using the same method as above. The selectivity of NPs was evaluated using

the selectivity index (SI), defined as the ratio of IC_{50} (the concentration required to inhibit 50% of cell growth) in normal cells to that in tumour cells:

$$\text{Selectivity Index (SI)} = \frac{IC_{50,normal}}{IC_{50,tumour}} \quad (3)$$

where IC_{50} values were either directly obtained from the cell viability curves or calculated using nonlinear curve fitting with the sigmoidal logistic function based on the cell viability data [30].

During analysis, we found that 50% inhibition was not reached in HUVECs within the tested concentration range. Therefore, IC_{50} values for HUVECs could not be reliably determined and are reported as being greater than the maximum tested DOX-equivalent concentration.

2.9. Cell uptake and intracellular distribution

MDA-MB-231, 4T1 and HUVECs cells were used as the tumour and normal cell models to investigate the cell uptake and DOX distribution by comparison. The no FBS DMEM medium containing Fe_3O_4-DOX@GC NPs at different DOX concentrations of 20 and 50 μg/mL was incubated with adhered MDA-MB-231, 4T1 and HUVECs cells in a 24-well glass-bottom plate. After 6 h, the cells were washed with PBS three times and then fixed by 4% paraformaldehyde for 20 min, then washed again. Cell nuclei were stained with 4′,6-diamidino- 2-phenylindole (DAPI) and washed twice with PBS. Finally, the cell uptake was observed using a fluorescence microscopy (Zeiss Axio Observer Z1 Inverted Microscope).

2.10. 3D cell spheroid culture

A 3D tumour spheroid model was produced by the hanging drop method. 30 μL of 3 - 7 × 10^4 MCF-7 cells (to produce different sizes of spheroids) in DMEM containing 20% FBS was seeded on the inverted lid of the 65 mm petri dish to form a drop, and 20 drops were produced per dish. The petri dish was filled with PBS to prevent the evaporation of drops. The lid was then inverted onto the dish and incubated at 37 °C/ 5% CO_2 for 4-6 days until formation of spheroids (observed by optical microscopy).

2.11. Penetration of NPs in 3D cell spheroid under static magnetic field (SMF)

The MCF-7 cell spheroid (diameter was around 700 μm) was placed in the bottom of each well of a 48-well plate and was then incubated with Fe_3O_4-DOX NPs, and Fe_3O_4-DOX@GC NPs at pH 7.4 and pH 6.8 of DMEM medium for 24 h (concentration of DOX was 6 μg/mL). To investigate the influence of SMF on the penetration efficacy of NPs, a magnet (210-240 mT, measured by a magnetometer) was placed under the 48-well plate where spheroids were located after 16 h incubation with Fe_3O_4-DOX NPs and Fe_3O_4-DOX@GC NPs at pH 6.8. Afterward, spheroids were incubated with SMF for another 8 h at 37 °C. Then, the spheroids were washed with PBS three times and transferred to a glass bottom confocal plate before being observed by a confocal laser scanning microscopy (CLSM, Zeiss, 880, Germany). The *Z*-stack function was used to scan the NPs in the whole 3D cell spheroids at different depths with a 5 μm scanning interval (10× objective). A 488 nm laser was used to excite the DOX in NPs, and the detection range was 530 - 600 nm. The images were analysed in the ImageJ software. The experiment was repeated three times.

2.12. Penetration of NPs in 3D cell spheroid under the combination of SMF and alternating magnetic field (AMF) control

The large MCF-7 cell spheroid (diameter was around 850 μm) was placed in the bottom of 35 mm petri dish with 2 mL of DMEM medium containing Fe_3O_4-DOX NPs and Fe_3O_4-DOX@GC NPs. The DOX concentration remained at 6 μg/mL. The spheroids were co-incubated with NPs for 16 h at first and followed for 6 h with SMF application. Then, the cell media were discarded and replaced with fresh media without NPs. Then, the petri dish was placed in AMF for 30 min (10 KA/ m, 111.1 KHz, 12.5 mT) and then placed back to SMF control for another 1.5 h at 37 °C to ensure the total spheroid incubation was 24 h. The control groups were spheroids that were still co-incubated with NPs under SMF control after fresh media were added. The penetration of the NPs in spheroids was observed by CLSM using the z-stack function (5 μm scanning interval, 10× objective). Channel information of CLSM: DOX (red, excitation = 488 nm, detection = 530-600 nm). The images were analysed in the ImageJ software. The experiment was repeated three times.

2.13. Mouse experiment model

Female BALB/c mice (4-6 weeks) were bought from Charles River. All animal procedures were performed under Home Office License and the approved project license (PP3769641) in accordance with the UK Animals Act 1986 following local rules. All mouse studies were approved by the University of Edinburgh Ethics Committee. A mouse breast cancer model was established by injecting 4T1 cells (1 × 10^6 cells) in 100 μL of PBS into the right flanks of six-week-old female BALB/ c mice. When the tumour volume reached about 100 mm^3, mice were randomly divided into different groups.

2.14. In vivo fluorescence imaging

4T1-bearing mice were randomly divided into 3 groups (n = 3 per group) and intravenously (i.v.) injected with different therapeutic agents at the equivalent Dox dose levels (2 mg/kg Dox eq.), i.e. (i) Free DOX, (ii) Fe_3O_4-DOX@GC NPs, (iii) Fe_3O_4-DOX@GC NPs + Mag (static magnetic field). To establish a SMF for tumour targeting, a cylindrical permanent magnet (a 6 mm diameter, 4 mm high, N42 neodymium magnet, ≈ 0.08–0.12 T total magnetic field intensity (Btot), when measured 3 mm above (approximately = radius of tumour model) the magnet using a magnetometer) was bound to the tumour site utilising the surgical tape for 2 h. The distribution of free DOX or DOX-loaded NPs in various organs of mice was monitored at 1, 6, and 24 h by using the In-Vivo Optima Imaging System (Biospace). Fluorescent intensity of DOX was quantified as the area of positive signals divided by the filed area using ImageJ.

2.15. In vivo antitumour efficacy

The 4T1-bearing mice with tumour volume reached about 100 mm^3 obtained according to the abovementioned procedures in 2.13 were randomly grouped (5 per group). 100 μL of the respective aqueous therapeutic agents with equivalent DOX dose levels (2 mg/kg DOX eq.), namely (i) free DOX, (ii) Fe_3O_4-DOX@GC NPs, (iii) Fe_3O_4-DOX@GC NPs + Mag (static magnetic field), were given intravenously to each mouse via the tail vein. To provide SMF for treatment, a cylindrical permanent magnet (a 6 mm diameter, 4 mm high, N42 neodymium magnet) was non-invasively bound to the tumour site utilising the surgical tape for 2 h after 5 min post-injection. PBS (100 μL) was used as negative control. Treatments were given every other day for five doses. The tumour volume (V) was calculated using the formula $V = (a^* b^2)/2$ (mm^3), where (a) and (b) are the major and minor axes of the tumour measured by a calliper. The body weight of each mouse was measured and recorded during treatment as an index of systemic toxicity. The mice were euthanised after 9 days, and tumours were dissected and weighed. The main organs including heart, liver, spleen, lung and kidney were separated and fixed in formaldehyde for histological examination. Animals were also euthanised when showing signs of imperfect health (e.g., skin ulceration or inability to perform normal activity) or when the single tumour volume reaches over 1000 mm^3 during the experiment

periods.

To quantify the combination effect of nanoparticle chemotherapy and magnetic actuation in vivo, we applied the Bliss independence model [31] to tumour growth inhibition (TGI) on defined treatment day (day 9).

TGI for each group was calculated as:

$$\text{Tumour Growth Inhibition (TGI)} = 1 - \frac{\left(\Delta V_{\text{day N}} - \Delta V_{\text{day 0}}\right)_{\text{treated}}}{\left(\Delta V_{\text{day N}} - \Delta V_{\text{day 0}}\right)_{\text{control}}} \quad (4)$$

where $\Delta V_{control}$ denotes the changed tumour volume of the PBS group, $\Delta V_{treated}$ denotes the changed tumour volume of the free DOX, NPs only (without magnetic actuation) or NPs with magnetic actuation, respectively.

The Bliss-expected TGI ($TGI_{Bliss,exp}$) and the Bliss combination index (CI_{Bliss}) were calculated as:

$$CI_{Bliss} = \frac{TGI_{Bliss,exp}}{TGI_{Obs}} = \frac{TGI_A + TGI_B - TGI_A \times TGI_B}{TGI_{Obs}} \quad (5)$$

where TGI_A denotes the TGI of the NPs without magnetic actuation, TGI_B denotes the TGI of the free DOX group, and TGI_{Obs} denotes the TGI of the NPs with magnetic actuation.

2.16. Flow cytometry analysis

Tumours collected from mice were divided into small pieces and homogenised in cold digestion medium (DMEM supplemented with 100 μg/mL DNase I, 100 μg/mL Liberase TL, 100 μg/mL Liberase DM) and incubated on a shaker at 37 °C, 700 rpm for 30 min. Digested samples were filtered through 35 μm strainers, lysed for red blood cells using red blood cell lysis buffer (420,301; BioLegend), blocked with CD16/32 Abs (1:200; BD Bioscience), and stained for a combination of the following antibodies (Abs): CD45 (30-F11, #103116; BioLegend), CD11b (M1/70, #101241; BioLegend), Ly-6C (HK1.4, #128033; BioLegend), Ly-6G (1A8, #127641; BioLegend), F4/80 (BM8, #123146; BioLegend), PD-L1 (MIH6, # 153614; BioLegend), MHC-II (M5/114.15.2, #107622; BioLegend), CD86 (GL-1, #105006; BioLegend), CD206 (C068C2, #141706; BioLegend), CD3 (17A2, #100246; BioLegend), NK1.1 (PK136, #108735; BioLegend), CD4 (GK1.5, #100412; BioLegend), CD8a(53-6.7, #100730; BioLegend), CTLA-4 (UC10-4B9, #106314; BioLegend) and PD1 (MH5A, #143706; BioLegend). DAPI or Viability Dye EF450 (65-0863-18, eBioscience) was used to exclude dead cells. Cells were analysed on Fortessa 6 Laser (BD Bioscience).

2.17. Histological and immunofluorescence staining

Primary tumours and major organs (heart, liver, spleen, lung and kidney) were fixed by 4% PFA overnight and embedded in paraffin. Sections with thickness of 5 μm were dewaxed by xylene, antigen-retrieved in citrate buffer (pH 6.0), blocked with 5% bovine serum albumin (BSA) for 30 min at room temperature, and incubated with primary Abs against Iba1 (EPR16588, 1:300, #ab178846, Abcam), CD8a (5H10-1, 1:200, #100801, BioLegend), or Ki-67 (OTI5D7, 1:100, #ab156956, Abcam) in a wet chamber overnight at 4 °C. On the next day, sections were incubated with AF555-conjugated (1:200, A-31572; Invitrogen) or AF488- conjugated secondary Abs (1:200, A-212208; Invitrogen). Nuclei were counterstained by DAPI. Images were taken by Zeiss Axio Observer microscope. Paraffin sections of the tumours and major organs were stained with hematoxylin and eosin (H&E) and then visualised using the automatic Zeiss Axioscan.

2.18. Blood compatibility assay

Fresh anticoagulant mouse blood was collected. Red blood cells (RBCs) were isolated by centrifugation at 3000 rpm for 10 min and then diluted with PBS (volume ratio was 1:50) for use. To test hemolytic activity, 500 μL of the diluted Fe_3O_4-DOX@GC NP PBS suspension were added to 500 μL of the diluted RBC suspension to achieve final DOX concentrations of 1, 10, 50, and 100 μg/mL. The suspension was vortexed briefly and incubated at 37 °C for 1 h. After incubation, the mixture was centrifuged at 3000 rpm for 10 min, and the concentration of released hemoglobin in the supernatant was quantified by the UV–Vis analysis (OD at 570 nm). The negative and positive control groups were prepared by incubation of 500 μL of the diluted RBC suspension with 500 μL of PBS and pure water, respectively. The absorbance of NPs (OD at 570 nm) at each test concentration was also measured as the NP background control. Each test was carried out in three replicates, and the results were expressed as the hemolysis ratio

$$\text{Hemolysis ratio (\%)} = \frac{OD_{sample} - OD_{NP\_background} - OD_{negative}}{OD_{positive} - OD_{negative}} \times 100 \quad (6)$$

2.19. Iron tracking by Prussian blue staining

Paraffin sections of the tumours were dewaxed by xylene (2 × 10 min) and rehydrated in a series of ethanol solutions (100%, 95%, 90%, 80% and 70%, 5 min for each), and deionised water (5 min). The Fe_3O_4 NPs in tumour sections were stained with the mixture of 10% potassium ferrocyanide and 20% HCl (1:1 volume mix) for 30 min and washed twice with water. The cytoplasm was counterstained with 0.1% nuclear fast red for 10 min and rinsed with water. All slides were mounted in PermaFluor mounting medium (Epredia™ TA-030-FM) with coverslips and observed by Zeiss Axio Observer microscope.

2.20. Statistical analysis

All experimental data shown were generated using GraphPad Prism software (v8) or Origin (v8) and displayed as mean and standard deviations (SD) for at least three independent experiments. Statistical comparisons were performed using two-tailed unpaired Student's *t*-test and ANOVA followed by multiple comparison tests. P value <0.05 was considered statistically significant.

3. Results and discussion

3.1. Preparation and characterisation of magnetic Fe_3O_4-DOX NPs

In this study, uniform and ultra-small OA-Fe_3O_4 NPs with a spherical morphology and an average size of 10 ± 1 nm were synthesised (Fig. S1a). Saturation magnetisation of OA-Fe_3O_4 NPs was 50 emu/g (Fig. S1b). To fabricate self-assembled Fe_3O_4-DOX NPs, a solvent exchange nanoprecipitation method was employed. In this process, an organic solvent mixture containing OA- Fe_3O_4 NPs and hydrophobic DOX molecules (see 2.3) was injected into an anti-solvent (water). The sudden change in solvent environment, combined with hydrophobic interactions, drove the self-assembly of DOX molecules and OA-Fe_3O_4 NPs into Fe_3O_4-DOX NPs.

As shown in Fig. 1a, pure DOX NPs (without Fe_3O_4 NPs) exhibited an average size of 81.4 ± 25.5 nm. For synthesizing magnetic drug NPs by solvent exchange method, we found that organic solvent composition is crucial for the spatial distribution of Fe_3O_4 NPs in the pure DOX NPs. When THF was the organic solvent, the Fe_3O_4 NPs were attached to the surface of the DOX NPs (Fig. S2a). When organic solvent is the mixture of THF and DMF with 4:3 or 3:3 volume ratio, the small Fe_3O_4 NPs and DOX self-assembled separately (Fig. S2b, c). However, when the organic solvent was changed to THF: DMF = 1: 10, the Fe_3O_4 NPs were embedded in the matrix of DOX NPs rather than on the surface (Fig. 1b, termed as Fe_3O_4-DOX NPs). The reason for different spatial configurations is that OA-Fe_3O_4 NPs are more hydrophobic than DOX. When the solvent was THF (polarity index = 4) [32], the solubility of OA-Fe_3O_4 NPs is higher than DOX. Thus, after dropping into water, the DOX NPs formed rapidly before OA-Fe_3O_4 NPs aggregated [33]. However, in a

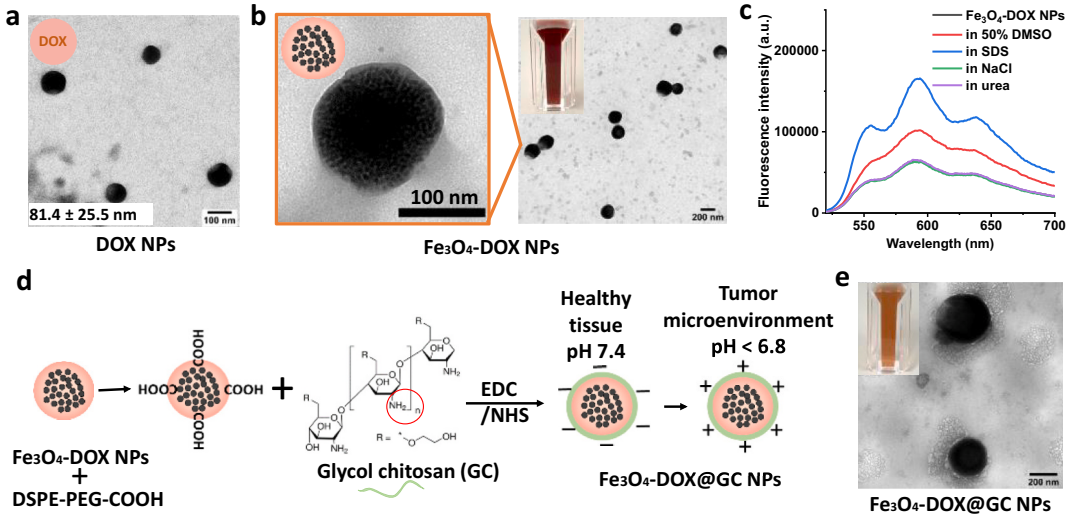

Fig. 1. Characterisation of Fe_3O_4-DOX NPs. a The TEM image of pure DOX NPs. b TEM images of Fe_3O_4-DOX NPs (weight ratio of DOX: OA-Fe_3O_4 = 1:2) and representative TEM image of one single NP. c The fluorescent spectrum of Fe_3O_4-DOX NPs in different buffer solutions. d Schematic illustration of GC surface modification on Fe_3O_4-DOX NPs, enabling tumour microenvironment-responsive charge reversal (negative to positive). e TEM images of GC-coated Fe_3O_4-DOX NPs, with insets showing respective aqueous dispersions.

more polar solvent, DMF (polarity index = 7.2), the solubility of DOX is higher than that of OA-Fe_3O_4 NPs, which slows down the precipitation of DOX NPs. In this case, the OA-Fe_3O_4 NPs are aggregated as the core at first, and then DOX molecules encapsulate the core and form magnetic drug NPs.

The representative Fe_3O_4-DOX NP (1:2 ratio) in Fig. 1b show an overall size of 225 ± 38.8 nm, and a thin PEG coating (7.5 ± 2.2 nm). Given that a single OA-Fe_3O_4 NP has a diameter of 10 nm and the volume fraction packing of spheres is 74% [34], the representative Fe_3O_4-DOX NP with 225 nm of average size is estimated to contain approximately 6853 OA-Fe_3O_4 NPs in its core area based on volume ratio calculation. Importantly, since the magnetic force exerted by an external magnetic field on magnetic NPs is proportional to their volume (assuming constant magnetisation), the prepared Fe_3O_4-DOX NPs are capable of generating a greater motive force, approximately 6853 times that of individual OA-Fe_3O_4 NPs under the same magnetic field, which is critical for magnetic targeting applications.

The effect of varying feed ratios of DOX to Fe_3O_4 NPs on the morphology and size of the resulting NPs was also investigated. As shown in Fig. S3, all NPs exhibited similar morphologies, but their sizes increased with lower DOX-to-Fe_3O_4 ratios, ranging from 112 to 225 nm. The corresponding hydrodynamic sizes are summarised in Table S1.

To elucidate the assembly mechanism of Fe_3O_4-DOX NPs, the NPs were incubated with urea (to disrupt hydrogen bonds), NaCl (to disrupt electrostatic interactions), and SDS (to disrupt hydrophobic interactions), followed by fluorescence analysis. Fe_3O_4-DOX NPs exhibited quenched fluorescence due to DOX aggregation, but fluorescence was restored upon dissociation in 50% DMSO (Fig. 1c). Notably, fluorescence recovery was observed only after the addition of SDS, while urea and NaCl had no significant effect. These results demonstrate that hydrophobic interactions are the primary driving force in the formation of Fe_3O_4-DOX NPs, with minimal contributions from hydrogen bonding or electrostatic interactions.

3.2. Surface functionality of Fe_3O_4-DOX NPs with charge reversal coating

The design and preparation of charge-reversal Fe_3O_4-DOX NPs are illustrated in Fig. 1d. DSPE-PEG-COOH served dual roles: stabilising Fe_3O_4-DOX NPs and acting as a linker for GC via amidation, yielding Fe_3O_4-DOX@GC NPs. The GC coating enables surface charge conversion from negative to positive in acidic tumour microenvironments. Zeta potential measurements at varying pH and GC:DSPE-PEG-COOH ratios (Fig. S4a) revealed that increasing GC content elevated NP surface charge across all pH conditions. At a 1:5 DSPE-PEG-COOH:GC ratio, Zeta potential shifted from −1.9 mV (pH 7.4) to +3.0 mV (pH 6.5). In contrast, uncoated Fe_3O_4-DOX NPs remained negatively charged (−10 to −20 mV) at pH 5.0–7.4.

Fig. S4b shows UV–Vis spectra of Fe_3O_4-DOX NPs with varying DOX: Fe_3O_4 ratios. OA- Fe_3O_4 NPs exhibited broad absorption (200–550 nm), while DOX aggregation in Fe_3O_4-DOX NPs caused a redshift from 482 nm (free DOX) to 499 nm. At a 1:2 DOX:Fe_3O_4 ratio, NPs displayed distinct Fe_3O_4 absorption bands and sufficient Fe content (~6853 Fe_3O_4 NPs per NP) to generate magnetic force under a field (Fig. S4c). This ratio was selected for further studies, with DOX encapsulation efficiency (DEE) at 94% for Fe_3O_4-DOX NPs. GC coating reduced DEE to 64.2% due to washing-induced drug loss, evidenced by diminished DOX absorbance (Fig. S4d). Despite this reduction, Fe_3O_4-DOX@GC NPs still exhibited a high drug loading efficiency (LE) at 69%. TEM confirmed Fe_3O_4-DOX@GC NPs retained spherical morphology and monodispersity (Fig. 1e), with sizes of 237 ± 68.7 nm. DLS revealed hydrodynamic sizes of 284.8 ± 4 nm (PDI = 0.172) and 362.1 ± 6.5 nm (PDI = 0.365) for uncoated and coated NPs, respectively (Fig. S4e). Drug release studies (Fig. S4f) under physiological (pH 7.4), tumour microenvironment (pH 6.5), and intracellular (pH 5.0) conditions showed sustained release over 400 h, indicating homogeneous DOX encapsulation. Faster release at pH 5.0 was attributed to chitosan swelling in acidic environments [35]. To better simulate physiological conditions, the drug release profile was further examined in DMEM containing 10% FBS. As shown in Fig. S4g, a sustained release phase was observed, initiating after approximately 50 h in this medium. This delayed release indicates that interactions between serum proteins and the nanoparticle surface likely modulate drug diffusion, resulting in a more gradual and prolonged release under in vivo-like conditions.

3.3. pH-dependent and tumour cells-targeted cytotoxicity of Fe_3O_4-DOX@GC NPs

MDA-MB-231 (triple-negative breast cancer) cells were used to evaluate cytotoxicity at pH 7.4 and 6.8 (adjusted with lactic acid; Fig. S5). Mild acidity slightly enhanced cell proliferation (Fig. S6). At pH 7.4, free DOX showed higher toxicity than NPs (Fig. S7a). At pH 6.8, free DOX toxicity decreased, while Fe_3O_4-DOX@GC NP toxicity

increased and became higher than free DOX (@GC NPs vs. free DOX = 50% vs. 56% viability at 10 μg/mL DOX; Fig. S7b), likely due to charge-switching to positive, enhancing cellular affinity. The IC_{50} values of Fe_3O_4-DOX@GC NP against MDA-MB-231 cells at pH 7.4 and pH 6.8 were determined to be 38.6 and 9.6 μg/mL (DOX concentrations), respectively. Uncoated Fe_3O_4-DOX NPs reduced viability by <15% regardless of pH, confirming GC coating improves efficacy in acidic, proliferative microenvironments. Thus, the results confirmed that surface modification with GC can improve the anticancer efficacy of magnetic drug NPs in the cell proliferation-facilitated environment (pH 6.8) via the pH-responsive charge reversal property.

Next, the cytotoxicity of Fe_3O_4-DOX@GC NPs was further evaluated using both 4T1 and HUVECs cells as representative tumour and normal cell models, respectively. As illustrated in Fig. S7c, d, Fe_3O_4-DOX@GC NPs also exhibited toxicity toward 4T1 tumour cells, while showing almost non-toxic to HUVECs from 1 to 10 μg/mL DOX. Furthermore, data from Fig. S8 indicated that Fe_3O_4 NPs alone possessed minimal toxicity to tumour cells even at elevated concentration. These results confirmed that the observed antitumor efficacy is primarily attributable to the released DOX.

Cellular uptake analysis revealed that 4T1 and MDA-MB-231 cells internalised significantly higher levels of Fe_3O_4-DOX@GC NPs than HUVECs (Fig. S9). Notably, a portion of the nuclear localisation of Fe_3O_4-DOX@GC NPs was observed within the nuclei of 4T1 and MDA-MB-231

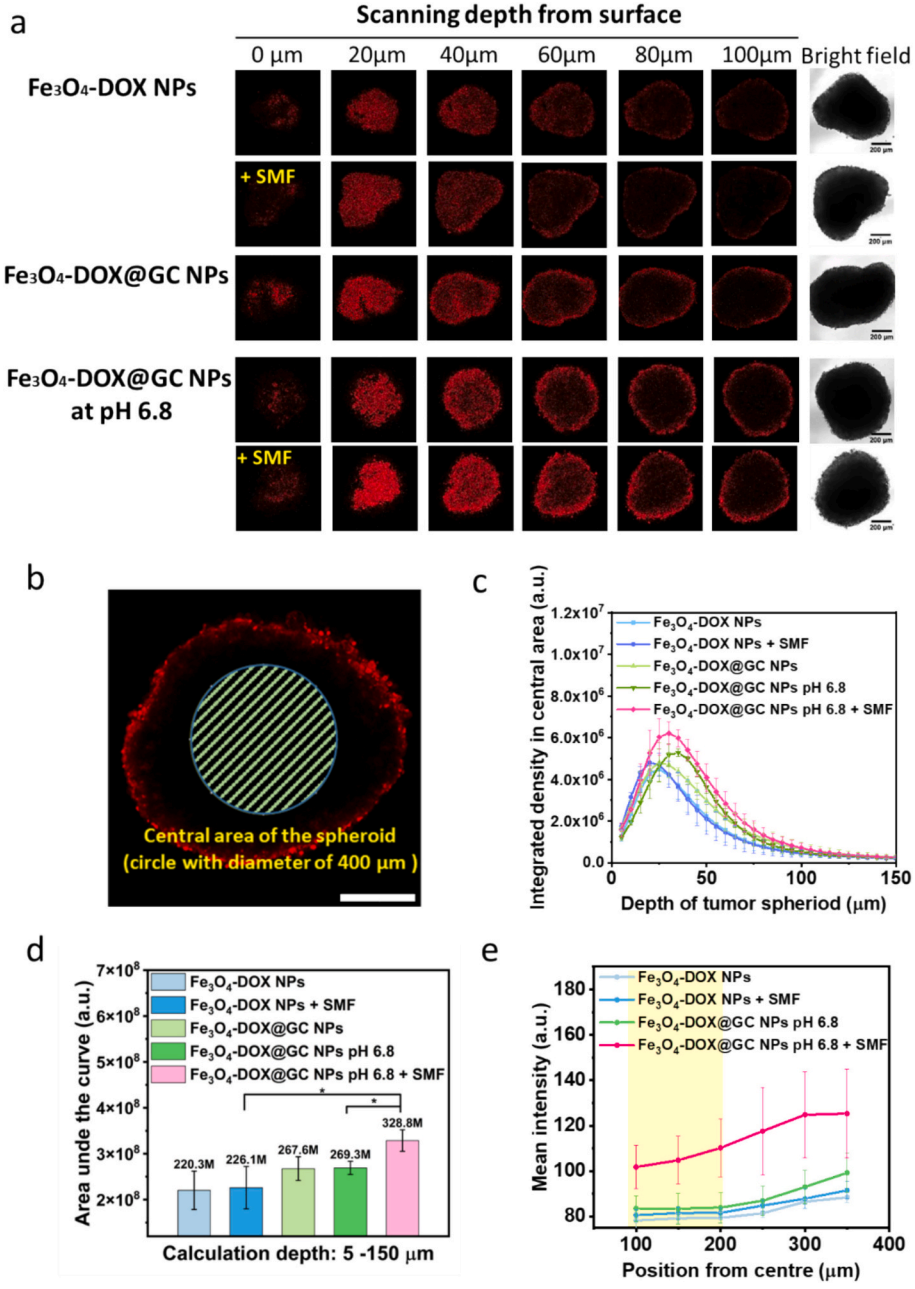

Fig. 2. Tissue penetration profiles of Fe_3O_4-DOX NPs and Fe_3O_4-DOX@GC NPs under SMF direction at different pH conditions. a Bright-field and fluorescence images of transverse spheroid sections (0-100 μm depth) after 24 h NP incubation. SMF-treated groups are marked '+SMF'. Red fluorescence indicates DOX in NPs. Scale bar: 200 μm. b Measurement strategy: A central 400-μm diameter circular area was selected for NP accumulation quantification to exclude surface DOX signals. Scale bar: 200 μm. c Integrated DOX fluorescence density across spheroid depths (5-μm intervals). d Area under the curve of the integrated density in central area calculated from (c) for 5-150 μm depths. e DOX fluorescence intensity profiles from spheroid centre to edge at fixed 100-μm depth (yellow background indicates central region). Three spheroids were analysed per group (additional images in Fig. S10). Data represent mean ± SD (*$P < 0.05$).

cells, whereas minimal nuclear accumulation was detected in HUVECs. Collectively, these findings indicate that Fe_3O_4-DOX@GC NPs exhibit enhanced tumour-cell uptake and partial nuclear delivery, supporting their potential as effective chemotherapeutic formulations with reduced off-target toxicity.

3.4. Magnetic field enhanced penetration in 3D tumour spheroids

The GC-coated NPs could transform into positive surface charges that obtain higher cellular internalisation and may penetrate deeper into tumour tissue than NPs with negative charges [36]. In addition, the magnetic driving force could be an effective power to promote the penetration of magnetic NPs. To prove these experimentally, MCF-7 cells were used to culture compact 3D cell spheroids to mimic the tumour tissue. Spheroids were then incubated with Fe_3O_4-DOX and Fe_3O_4-DOX@GC NPs, respectively, and observed under confocal microscopy. To explore the dynamic charge transformability- and magnetic drive-dual enhanced penetration, tumour microenvironment was constructed by modulating the pH of cell spheroids incubation medium to 6.8. A permanent magnet was used to provide a static magnetic field (SMF). The stronger red fluorescence of DOX was observed for magnet-applied NPs groups (two groups labelled with '+ SMF') when compared to their corresponding groups without SMF direction, and Fe_3O_4-DOX@GC NPs at the acidic environment and upon SMF applied showed greater fluorescence at each depth for both periphery and central areas than all other groups (Fig. 2a). To investigate this behaviour quantitatively, we quantified the fluorescence intensity of DOX for each depth but only counted signals from the central area of the spheroids (a fixed circular area with a diameter of 400 μm) to analyse the NPs that penetrated into the interior area (Fig. 2b). The quantised results confirmed that GC coating and SMF propulsion significantly enhanced the penetration capability of NPs at pH 6.8. Then the area under the curve of each curve in Fig. 2c was calculated, which could reflect the total retention of NPs in the central area of the tumour tissue from the depth of 5 to 150 μm. As shown in Fig. 2d, compared to the DOX retention from Fe_3O_4-DOX NPs in tumour tissue, GC-coated NPs demonstrate a 22% increase in DOX retention at pH 6.8. This enhancement rises to 49% when both GC modification and SMF direction are applied simultaneously at the same pH.

When the scanning depth was fixed at 100 μm, the Fe_3O_4-DOX@GC NPs (pH 6.8) + SMF group displayed the highest fluorescence intensity from the spheroid centre to its periphery (Fig. 2e). Both strategies - the slightly acidic environment-induced positive charge switch of the GC coating and SMF direction - independently enhanced the penetration of magnetic drug NPs. Their combination produced a synergistic effect that maximised NP penetration. Notably, the SMF direction-induced penetration improvement was more pronounced for Fe_3O_4-DOX@GC NPs (pH 6.8) than for Fe_3O_4-DOX NPs, suggesting that the initial accumulation of NPs in tumour tissue is crucial for efficient magnetically directed penetration.

3.5. Combination of SMF and AMF application enhances NP penetration in 3D tumour spheroids

Previous sections in this study have demonstrated that SMF improve the penetration of magnetic NPs into tumour tissue. To further enhance penetration, we combined SMF with an AMF, which induces NP vibration to help overcome the high resistance posed by tumours' compact and heterogeneous structure. This dual-field approach was designed to synergistically enhance NP penetration: SMF was first applied to drive NPs into tumour tissue, followed by AMF to agitate the NPs, and then SMF was reapplied to guide their further movement. Fluorescence imaging of transverse sections and 3D reconstructions revealed greater accumulation of both Fe_3O_4-DOX and Fe_3O_4-DOX@GC NPs in spheroid cores under combined SMF + AMF treatment compared to SMF alone (Fig. 3a). Notably, spheroids treated with GC-coated NPs at pH 6.8 exhibited significant swelling, reflecting DOX-induced toxicity and confirming effective NP penetration. The consequent widespread cell death disrupted the spheroid's compact architecture. This effect was most pronounced in the SMF + AMF group, where Fe_3O_4-DOX@GC NP-treated spheroids developed a looser structure with visible gaps in 3D reconstructions, unlike the more compact morphology seen with SMF alone. Quantitative analysis of DOX fluorescence intensity across spheroid depths demonstrated that the combined magnetic field system

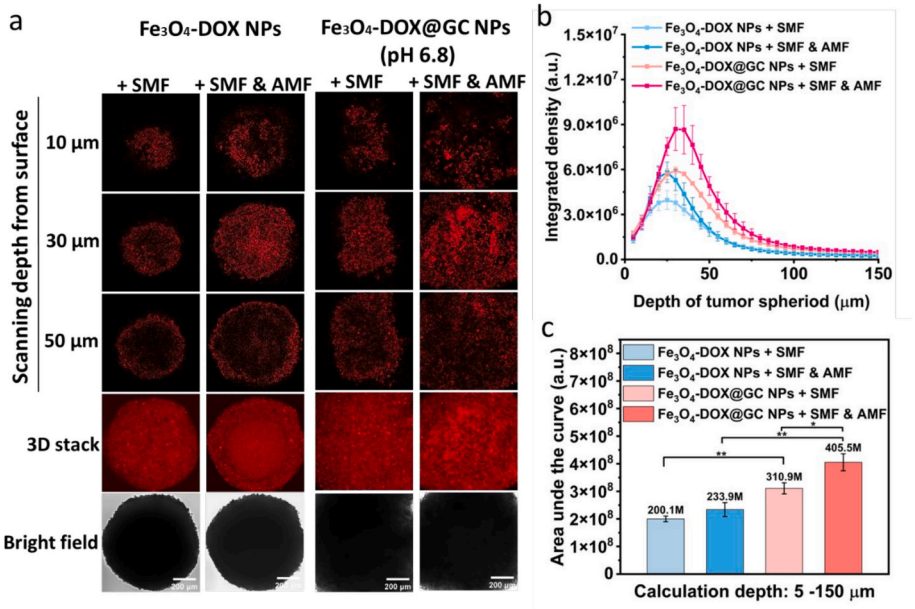

Fig. 3. Enhanced tissue penetration of Fe_3O_4-DOX NPs and Fe_3O_4-DOX@GC NPs under combined SMF and AMF direction. a Bright-field and fluorescence images of transverse spheroid sections (10–50 μm depth) and 3D reconstructions (0–300 μm depth, 5-μm intervals). Red fluorescence indicates DOX-loaded NPs. Scale bar: 200 μm. b Integrated DOX fluorescence density in central spheroid regions (500-μm diameter circular area) across sequential depths (5-μm intervals). c Area under the curve calculated from panel b for depths of 5–150 μm. Three spheroids were analysed per group (additional images in Fig. S11). Data represent mean ± SD (*$P < 0.05$, **$P < 0.01$).

enhanced penetration for both NP types versus SMF alone (Fig. 3b). Specifically, SMF + AMF treatment increased DOX accumulation from Fe_3O_4-DOX@GC NPs by approximately 30% over SMF alone, and by 103% compared to Fe_3O_4-DOX NPs with SMF (5–150 μm depth range; Fig. 3c). These results establish that the combined magnetic field strategy significantly improves both tissue penetration and payload retention of magnetic NPs in 3D tumour models compared to single-field approaches.

3.6. In vivo magnetic targeting efficiency of NPs

To further investigate the therapeutic potential of Fe_3O_4-DOX@GC NPs, we utilised an experimental mouse tumour model, where 4T1 mouse mammary tumour cells are subcutaneously injected into the syngeneic BALB/c mice. When the tumour volume reached approximately 100 mm^3, free DOX and Fe_3O_4-DOX@GC NPs, at a DOX dose of 2 mg/kg, were administered intravenously (i.v.). Following the injection, a cylindrical magnet (6 mm in diameter) was applied to the tumour site for 2 h to provide a magnetic attraction force. Based on calculations, the actuation force on a Fe_3O_4-DOX@GC NP reached up to 11.5 fN as it passed through the tumour (SI document). At predetermined time points, the tumour and other organs were resected, and the biodistribution of DOX in the tissues were determined by fluorescence imaging. As shown in Fig. 4a, at all three evaluated time points (1 h, 6 h, and 24 h), the Fe_3O_4-DOX@GC + Mag group exhibited significantly stronger DOX fluorescence signals than the other two counterparts. Indeed, at 24 h post-injection, the intratumoural DOX signal of the Fe_3O_4-DOX@GC + Mag group displayed an approximately 2.0 ± 0.3-fold and 6.3 ± 0.8-fold increase compared to the Fe_3O_4-DOX@GC group and the free DOX group, respectively (Fig. 4b). It is worth noting that Fe_3O_4-DOX@GC NPs without magnetic field actuation showed prominent accumulation in the liver and kidneys, whereas the fluorescence signals of the Fe_3O_4-DOX@GC + Mag and free DOX groups were significantly lower in the liver during the first 6 h (Fig. 4c, d). These results demonstrate that magnetic-field-actuated targeting enhances tumour accumulation of Fe_3O_4-DOX@GC NPs by overriding reticuloendothelial system (RES)-mediated liver/spleen sequestration [37,38]. This reduces off-target deposition in healthy organs while significantly increasing DOX delivery to the tumour site.

3.7. In vivo tumour therapeutic outcomes of NPs in combination with magnetic targeting

Given the active tumour-targeting ability of the Fe_3O_4-DOX@GC + Mag group, we further evaluated the in vivo chemotherapeutic efficacy of Fe_3O_4-DOX@GC NPs. Based on the in vivo imaging results demonstrating persistent DOX fluorescence signals within tumours even 24 h post-injection under magnetic field actuation, we optimised the treatment regimen to five repeated administrations at two-day intervals, with a permanent magnet applied to the tumour site for 2 h following each injection (Fig. 5a). As shown in Fig. 5b, the Fe_3O_4-DOX@GC + Mag treatment significantly suppressed tumour growth compared to PBS or free DOX treatments. By day 9, the average tumour volume reached approximately 750 mm^3 in PBS-treated mice and 741 mm^3 in free DOX-treated mice, indicating that free DOX failed to inhibit tumour growth. In contrast, the tumour volume in Fe_3O_4-DOX@GC + Mag treated mice was markedly smaller (310 mm^3) than these groups, as well as mice treated with Fe_3O_4-DOX@GC without magnetic guidance (490 mm^3). Consistently, the tumour growth rates calculated relative to baseline volumes (day 0), and weights of excised tumours were significantly lower in the Fe_3O_4-DOX@GC + Mag treated mice (Fig. 5c-e). The Fe_3O_4-DOX@GC NPs alone demonstrated moderate tumour growth inhibition,

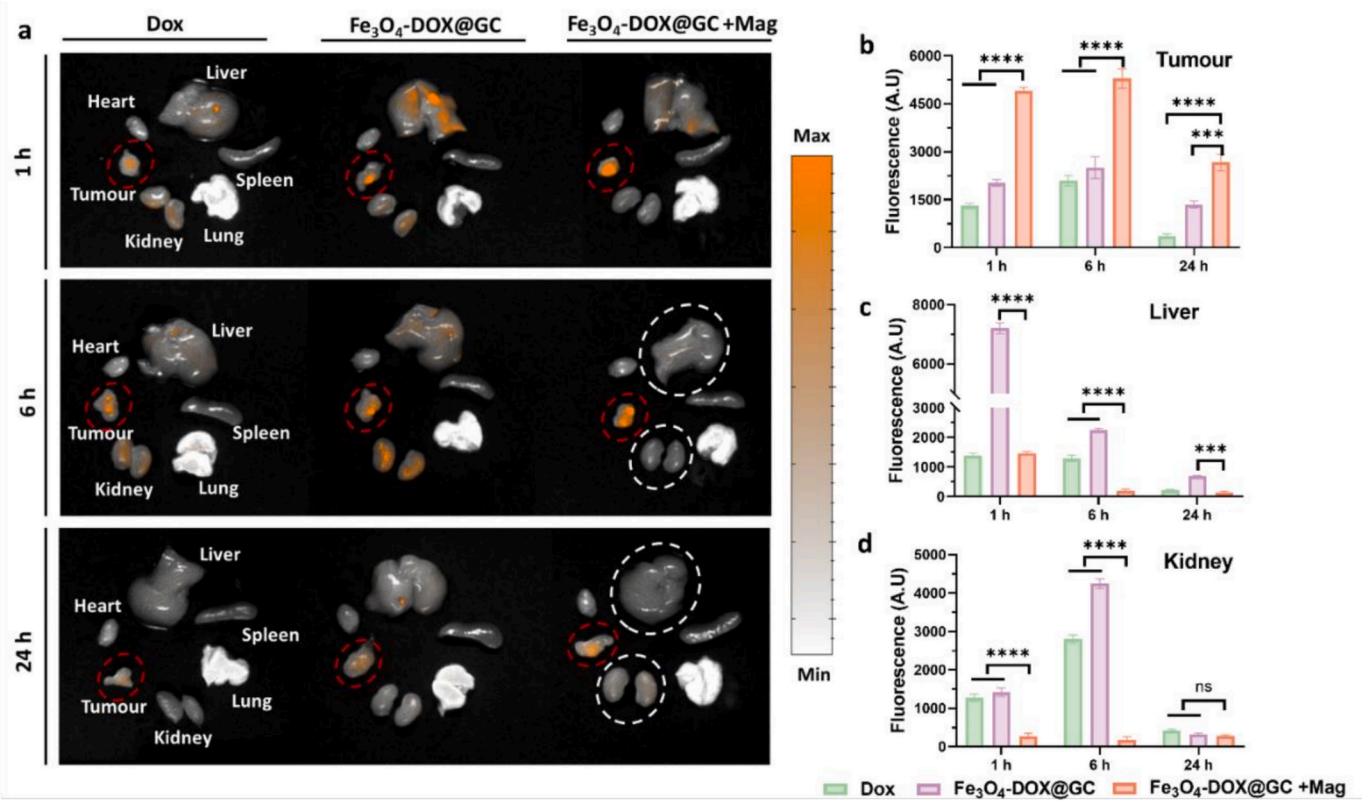

Fig. 4. Targeted delivery of designed nanoparticles (NPs) under a magnetic field.
a In vivo imaging of DOX and Fe_3O_4-DOX@GC NPs with or without magnetic field exposure across different organs. b-d Quantification of accumulated DOX from Fe_3O_4-DOX@GC NPs (with/without magnetic field) in: (b) tumour, (c) liver, and (d) kidney tissues. All data are presented as mean values ± standard deviation. ****$p < 0.0001$. ns: non-significant.

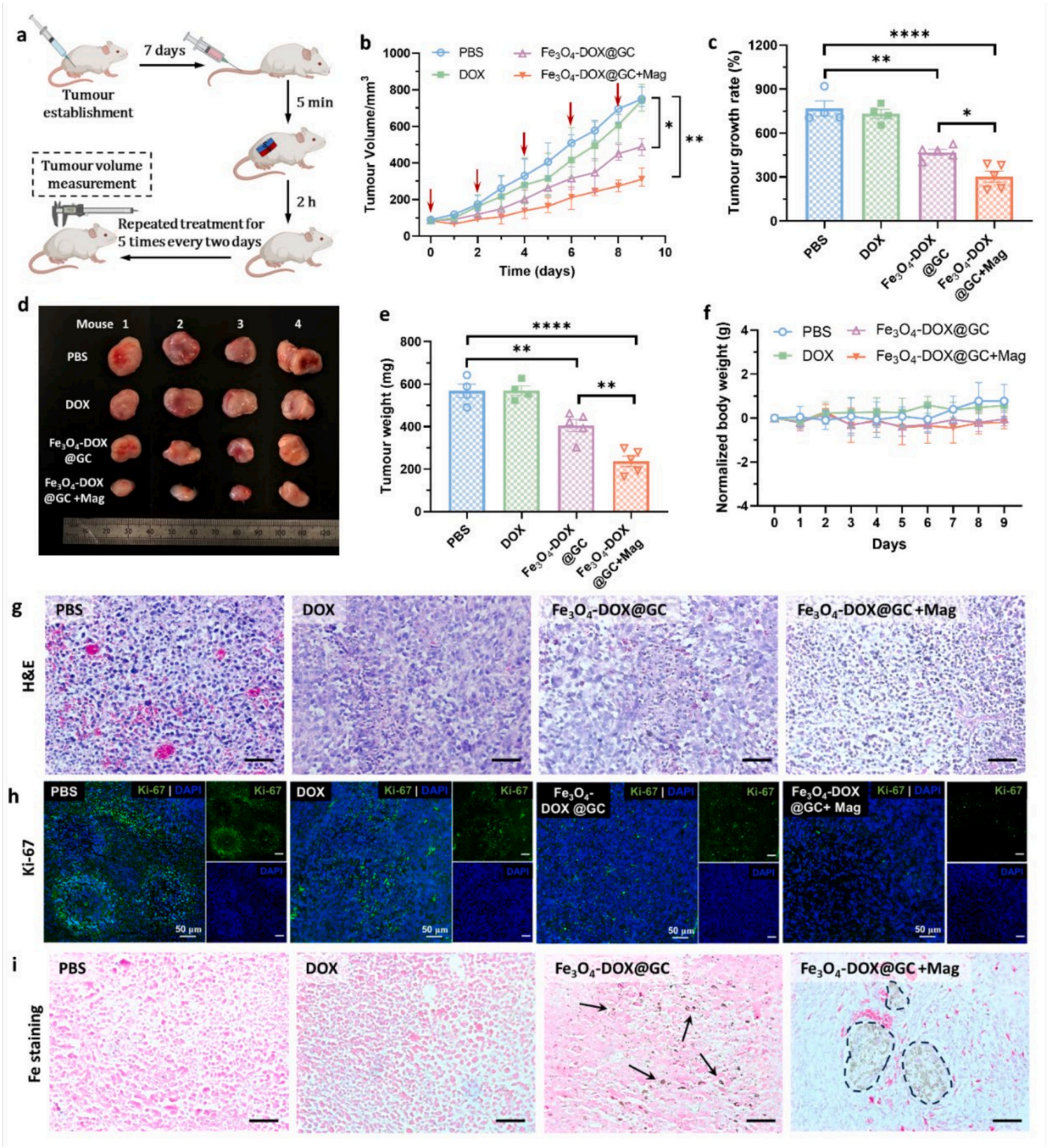

Fig. 5. In vivo anti-tumour efficacy of Fe_3O_4-DOX@GC NPs under magnetic actuation. a Treatment schedule for the 4T1 xenograft tumour model. b Tumour growth curves in 4T1-bearing mice after indicated treatments ($n = 5$). c Tumour growth rates across groups at the endpoint. d Excised tumours after treatment. e Weights of tumour tissues from the 4T1 model post-treatment. f Normalised body weights of mice during treatment. g H&*E*-stained tumour tissues collected on day 9 (scale bar: 50 μm). h Immunofluorescence microscopy of Ki-67 (green) and DAPI-counterstained nuclei (blue) in tumour sections. i Prussian Blue-stained NPs (dark brown) and nuclear fast red-stained cells (red) in tumour tissues (scale bar: 50 μm). *$p < 0.1$, **$p < 0.01$, ***$p < 0.001$, ****$p < 0.0001$. Error bars represent standard deviation.

whereas the combination with magnetic targeting significantly enhanced chemotherapeutic efficacy, achieving potent suppression of tumour progression. Importantly, no significant body weight changes were observed in any treatment group despite multiple injections, indicating negligible acute toxicity at the administered DOX dose (Fig. 5f). To quantify the synergistic effect of nanoparticle chemotherapy and magnetic actuation, the Bliss combination index (CI_{Bliss}) was calculated. A Bliss combination index (CI_{Bliss}) of <1 indicates synergy, $CI_{Bliss} = 1$ indicates additivity, and $CI_{Bliss} > 1$ indicates antagonism. Using the day-9 in vivo TGI data, a CI_{Bliss} value of 0.0068 ± 0.0013 was

obtained, indicating a marked synergistic effect between chemotherapy and magnetic actuation with Fe_3O_4-DOX@GC treatment. Notably, this pronounced synergy is accompanied by significant modulation of the tumour immune microenvironment, suggesting that immune-related mechanisms may further contribute to the observed therapeutic enhancement (as discussed in the next section). The H&E staining results (Fig. S13) also demonstrated that no apparent abnormality or lesion appeared in any of these major organs after treatments with Fe_3O_4-DOX@GC NPs. Furthermore, hemolytic activity assays confirmed the good blood compatibility of the Fe_3O_4-DOX@GC NPs, with hemolysis rates remaining below the ISO standard threshold of 5% (Fig. S14). All these results indicated that Fe_3O_4-DOX@GC NPs exhibit favourable in vivo biocompatibility and a reduced systemic toxicity profile compared to free DOX.

The histological H&E staining of tumour sections revealed extensive areas of sparse cells in the Fe_3O_4-DOX@GC + Mag group, suggesting substantial cell death induced by this treatment (Fig. 5g). The expression of Ki-67 immunostaining, a well-established marker of cellular proliferation [39], was lower in Fe_3O_4-DOX@GC-treated tumours compared to tumours treated with PBS or free DOX (Fig. 5h). Notably, the undetectable Ki-67 expression and disrupted tumour architecture found in the Fe_3O_4-DOX@GC + Mag group suggested effective proliferation blockade by higher drug penetration through this treatment. Prussian Blue staining was employed to visualise the distribution of iron NPs within the tissue. As expected, the substantial accumulation of NPs was observed in the tumour sections from the Fe_3O_4-DOX@GC + Mag group, indirectly verifying DOX distribution (Fig. 5i). These results demonstrate that the remarkable tumour suppression achieved with Fe_3O_4-DOX@GC + Mag treatment directly correlates with magnetic-field-enhanced tumour targeting. The improved NP accumulation facilitated prolonged DOX retention within tumours, thereby augmenting chemotherapeutic efficacy. The acid-responsive charge-reversal property imparted by the GC surface layer may have synergistically promoted deeper drug penetration into tumour tissue (in vivo data not shown), consistent with prior studies demonstrating enhanced tumour penetration via charge-reversal mechanisms [6,40]. However, passive

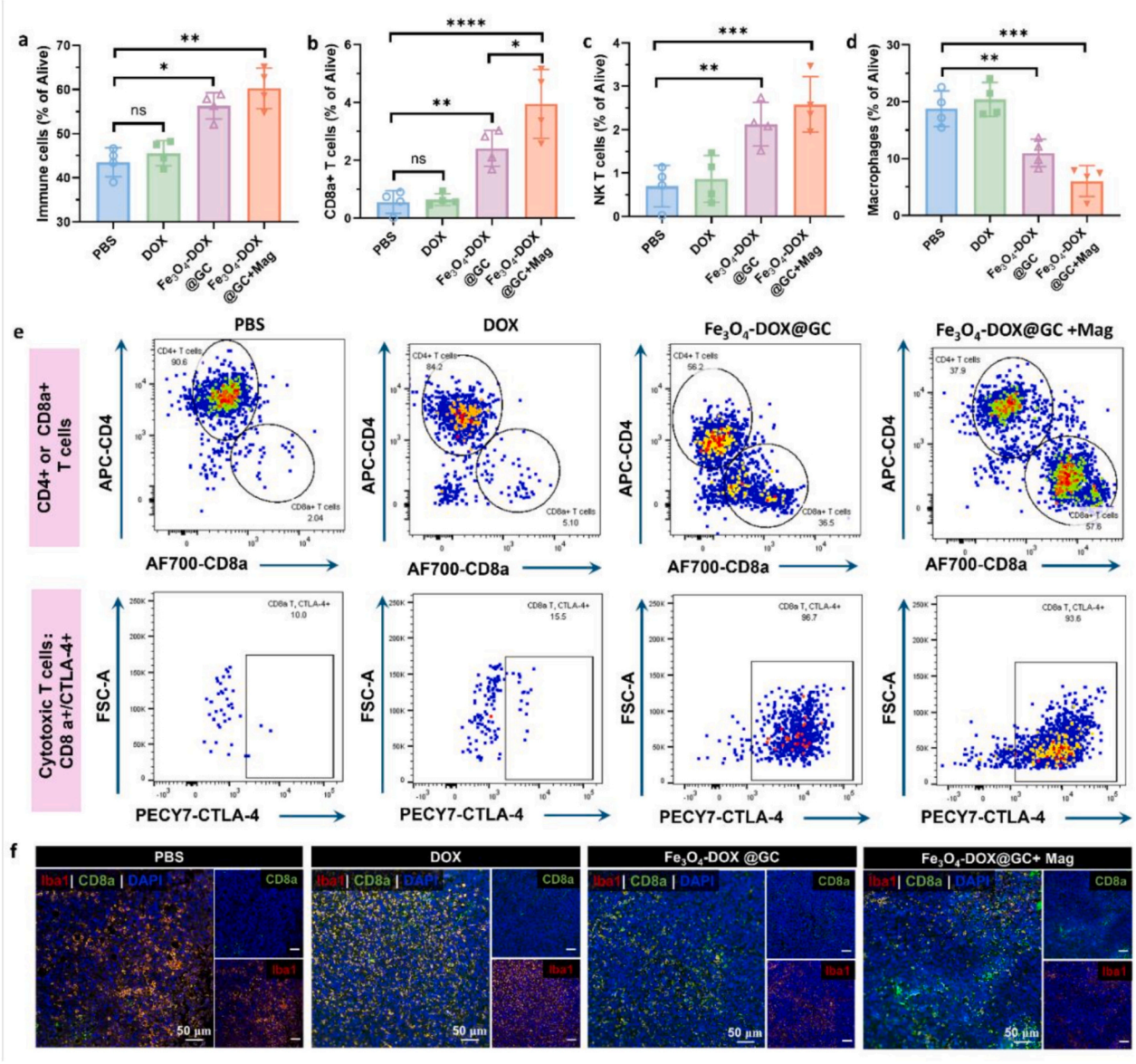

Fig. 6. Antitumour immunity induced by designed NPs in vivo with magnetic field actuation. a-d Flow cytometry analysis of immune cell subsets: (a) $CD45^+$ immune cells, (b) $CD8a^+$ T cells, (c) NK T cells, (d) macrophages. e Flow cytometry quantification of $CD8a^+$ T cell (top) and cytotoxic T ($CTLA\text{-}4^+$) cell (bottom) within tumour-infiltrating $CD8a^+$ T cell populations post-treatment. f Whole-mount immunofluorescence images of tumour samples (day 9) stained for $Iba1^+$ macrophages (Red), $CD8a^+$ T cells (green) and nucleus (blue). $^*p < 0.1$, $^{**}p < 0.01$, $^{***}p < 0.001$ and $^{****}p < 0.0001$. All error bars represent standard deviation.

delivery relying solely on the EPR effect proved insufficient for effective Fe_3O_4-DOX@GC accumulation in tumours (Fig. 5i), explaining the modest efficacy observed without magnetic actuation.

3.8. In vivo anti-tumour immune response of combination magnetic field actuation

Apart from directly interfering with DNA replication and transcription in tumour cells, leading to cytotoxic effects, DOX-mediated chemotherapy has been reported to induce immunogenic cell death (ICD) of tumour cells [41]. Furthermore, iron oxide NPs have been shown to inhibit tumour growth by regulating the polarisation of macrophages in tumour tissues [42]. Given the promising in vivo antitumour efficacy observed in the Fe_3O_4-DOX@GC + Mag treatment group, we investigated whether immune response activation contributes to its therapeutic mechanism. Flow cytometry analysis of intratumoural immune cell infiltration (Fig. 6a-d; gating strategy in Fig. S15, S16) revealed that tumours treated with Fe_3O_4-DOX@GC + Mag exhibited the highest frequencies of immune cells ($CD45^+$, 60.2 ± 4.7%) and lymphocyte subsets, including $CD8a^+$ T cells ($CD45^+CD3^+CD8a^+$, 3.9 ± 0.9%) and natural killer T (NKT) cells ($CD45^+CD3^+NK1.1^+$, 2.7 ± 0.6%). These populations were moderately low in the Fe_3O_4-DOX@GC group (without magnetic actuation) and markedly diminished in the free DOX group (45 ± 2.1%, 0.7 ± 0.1%, and 0.9 ± 0.4%, respectively), reaching levels comparable to the PBS control. This aligned with immunofluorescence staining (Fig. 6f), which showed pronounced $CD8a^+$ T cell (green) enrichment in Fe_3O_4-DOX@GC + Mag-treated tumours. The enhanced infiltration of immune-activating cells, particularly $CD8^+$ cytotoxic T lymphocytes, likely improved the immunosuppressive tumour microenvironment. However, $CD8^+$ T cells in Fe_3O_4-DOX@GC-treated groups showed elevated CTLA-4 expression by the endpoint (Fig. 6e), probably due to the chronic antigen exposure driving exhaustion. This checkpoint upregulation likely impairs T cell cytotoxicity, partially explaining the observed incomplete tumour eradication [43]. Combining CTLA-4 inhibitors with Fe_3O_4-DOX@GC + Mag therapy could synergistically sustain $CD8^+$ T cell function, which may be a focus for future studies.

Tumour-associated macrophages (TAMs), key immunosuppressive players in the tumour microenvironment [44,45] were significantly reduced in the Fe_3O_4-DOX@GC + Mag group (6.2 ± 2.5%) versus free DOX (20.3 ± 3.6%) and PBS (18.4 ± 3.9%) groups (Fig. 6d). Immunostaining for a pan-macrophage marker Iba1 (which colocalises with F4/80 [46]) confirmed sparse macrophage infiltration in Fe_3O_4-DOX@GC + Mag-treated tumours (Fig. 6f). Notably, pro-inflammatory macrophages ($F4/80^+CD86^+MHCII^+$) increased 2.9 ± 0.5-fold over PBS, while tumour-promoting subsets ($F4/80^+CD206^+PD\text{-}L1^+$) decreased tenfold (Fig. S17), suggesting TAM reprogramming. Iron oxide NPs may drive this shift via Fenton reaction-generated hydroxyl radicals (•OH) and reactive oxygen species (ROS), which induce cancer cell apoptosis and sustain pro-inflammatory macrophage polarisation through TNF-α/nitric oxide (NO) feedback loops [42,47]. Collectively, Fe_3O_4-DOX@GC + Mag therapy activates $CD8^+$ T cells, reduces TAM accumulation and reprograms TAMs toward an antitumoral phenotype, thereby ameliorating immunosuppression and enhancing tumour growth inhibition.

4. Conclusion

In summary, we have developed an active anticancer nanomedicine based-on Fe_3O_4-DOX@GC NPs that demonstrate controllable deep tumour penetration and advanced therapeutic efficacy in both 3D tumour models and in vivo systems. The nanomedicine integrates three key functionalities: (i) high capacity of hydrophobic drug and Fe_3O_4 particles encapsulation, (ii) multiple behaviours regulated by magnetic operations – NPs' distant translocation and local intratumoural penetration, and (iii) pH-induced surface charge reversal for active tumour targeting and drug release. Quantitative analysis showed that individual NPs generate clinically relevant actuation forces up to 11.5 fN under a 0.12 T magnetic fields, resulting a 6.3-fold increase in tumour accumulation compared with free DOX, alongside a 2.9-fold increase in pro-inflammatory macrophages. This treatment achieved superior tumour growth suppression relative to free drug controls (58% greater tumour volume reduction). Notably, the simple, carrier-free synthesis is adaptable to a wide range of hydrophobic drugs and readily scalable for industrial production. Our results offer both fundamental insights into magnetic nanoparticle behaviour in biological system and a practical framework of design, synthesis and actuation of multi-function nanomedicine toward their clinical translation.

CRediT authorship contribution statement

Xue Feng: Writing – review & editing, Writing – original draft, Validation, Methodology, Investigation, Formal analysis, Data curation, Conceptualization. **Hongdi Wang:** Writing – review & editing, Writing – original draft, Methodology, Investigation, Formal analysis, Data curation. **Yuxiang Xue:** Writing – review & editing, Data curation. **Nurbanu Ozgultekin:** Data curation, Formal analysis, Methodology, Writing – review & editing. **Takanori Kitamura:** Writing – review & editing, Supervision, Data curation. **Jin Li:** Writing – review & editing, Supervision, Data curation. **Defang Ouyang:** Writing – review & editing, Supervision. **Guangyu Zhu:** Writing – review & editing, Supervision. **Guangzhao Mao:** Writing – review & editing, Supervision. **Bin-Zhi Qian:** Writing – review & editing, Supervision, Funding acquisition, Data curation. **Xianfeng Chen:** Writing – review & editing, Validation, Methodology, Funding acquisition, Formal analysis, Data curation, Conceptualization.

Declaration of competing interest

The authors declare that they have no known competing financial interests or personal relationships that could have appeared to influence the work reported in this paper.

Acknowledgements

The authors would like to acknowledge Stephen Mitchell and David Kelly at the School of Biological Sciences Electron Microscopy unit for assistance with TEM and confocal microscopy. This research was funded in part by Wellcome Multi User Equipment Grant (WT104915MA), the Cancer Research UK Award (C47778/A30039), and MRC (MR/Y008448/1). For the purpose of open access, the author has applied a creative commons attribution (CC BY) license to any author accepted manuscript version arising.

Appendix A. Supplementary data

Supplementary data to this article can be found online at https://doi.org/10.1016/j.cej.2026.174177.

Data availability

Data will be made available on request.

References

[1] G. Batist, G. Ramakrishnan, C.S. Rao, A. Chandrasekharan, J. Gutheil, T. Guthrie, P. Shah, A. Khojasteh, M.K. Nair, K. Hoelzer, K. Tkaczuk, Youn Choi Park, L.W. Lee, Reduced cardiotoxicity and preserved antitumor efficacy of liposome-encapsulated doxorubicin and cyclophosphamide compared with conventional doxorubicin and cyclophosphamide in a randomized, multicenter trial of metastatic breast cancer, J. Clin. Oncol. 19 (2001) 1444–1454, https://doi.org/10.1200/JCO.2001.19.5.1444.

[2] D. Bobo, K.J. Robinson, J. Islam, K.J. Thurecht, S.R. Corrie, Nanoparticle-based medicines: a review of FDA-approved materials and clinical trials to date, Pharm. Res. 33 (2016) 2373–2387, https://doi.org/10.1007/S11095-016-1958-5.

[3] P. Lu, V.M. Weaver, Z. Werb, The extracellular matrix: a dynamic niche in cancer progression, J. Cell Biol. 196 (2012) 395, https://doi.org/10.1083/JCB.201102147.

[4] O. Trédan, C.M. Galmarini, K. Patel, I.F. Tannock, Drug resistance and the solid tumor microenvironment, J. Natl. Cancer Inst. 99 (2007) 1441–1454, https://doi.org/10.1093/JNCI/DJM135.

[5] L. Zhang, H. Su, Y. Liu, N. Pang, J. Li, X.R. Qi, Enhancing solid tumor therapy with sequential delivery of dexamethasone and docetaxel engineered in a single carrier to overcome stromal resistance to drug delivery, J. Control. Release 294 (2019) 1–16, https://doi.org/10.1016/J.JCONREL.2018.12.004.

[6] X. Feng, H. Dixon, H. Glen-Ravenhill, S. Karaosmanoglu, Q. Li, L. Yan, X. Chen, Smart nanotechnologies to target tumor with deep penetration depth for efficient cancer treatment and imaging, Adv Ther (Weinh) 2 (2019) 1900093, https://doi.org/10.1002/adtp.201900093.

[7] M.J. Ernsting, W.L. Tang, N.W. MacCallum, S.D. Li, Preclinical pharmacokinetic, biodistribution, and anti-cancer efficacy studies of a docetaxel-carboxymethylcellulose nanoparticle in mouse models, Biomaterials 33 (2012) 1445–1454, https://doi.org/10.1016/J.BIOMATERIALS.2011.10.061.

[8] Z. Duan, H. Cai, H. Zhang, K. Chen, N. Li, Z. Xu, Q. Gong, K. Luo, PEGylated multistimuli-responsive dendritic prodrug-based nanoscale system for enhanced anticancer activity, ACS Appl. Mater. Interfaces 10 (2018) 35770–35783, https://doi.org/10.1021/ACSAMI.8B12232.

[9] J. Zhao, S. Wu, J. Qin, D. Shi, Y. Wang, Electrical-charge-mediated cancer cell targeting via protein Corona-decorated superparamagnetic nanoparticles in a simulated physiological environment, ACS Appl. Mater. Interfaces 10 (2018) 41986–41998, https://doi.org/10.1021/ACSAMI.8B15098.

[10] T.D. Tailor, G. Hanna, P.S. Yarmolenko, M.R. Dreher, A.S. Betof, A.B. Nixon, I. Spasojevic, M.W. Dewhirst, Effect of pazopanib on tumor microenvironment and liposome delivery, Mol. Cancer Ther. 9 (2010) 1798, https://doi.org/10.1158/1535-7163.MCT-09-0856.

[11] Z. Li, X. Shan, Z. Chen, N. Gao, W. Zeng, X. Zeng, L. Mei, Applications of surface modification technologies in nanomedicine for deep tumor penetration, Adv. Sci. 8 (2021) 2002589, https://doi.org/10.1002/ADVS.202002589.

[12] Q. Zhou, S. Shao, J. Wang, C. Xu, J. Xiang, Y. Piao, Z. Zhou, Q. Yu, J. Tang, X. Liu, Z. Gan, R. Mo, Z. Gu, Y. Shen, Enzyme-activatable polymer–drug conjugate augments tumour penetration and treatment efficacy, Nat. Nanotechnol. 14 (2019) 799–809, https://doi.org/10.1038/s41565-019-0485-z.

[13] L. Dai, K. Li, M. Li, X. Zhao, Z. Luo, L. Lu, Y. Luo, K. Cai, L.L. Dai, K. Li, M.H. Li, X. J. Zhao, Z. Luo, L. Lu, Y.F. Luo, K.Y. Cai, Size/charge changeable acidity-responsive Micelleplex for photodynamic-improved PD-L1 immunotherapy with enhanced tumor penetration, Adv. Funct. Mater. 28 (2018) 1707249, https://doi.org/10.1002/ADFM.201707249.

[14] X. Xue, Y. Huang, R. Bo, B. Jia, H. Wu, Y. Yuan, Z. Wang, Z. Ma, D. Jing, X. Xu, W. Yu, T. Yin Lin, Y. Li, Trojan Horse nanotheranostics with dual transformability and multifunctionality for highly effective cancer treatment, Nat. Commun. 9 (2018) 1–15, https://doi.org/10.1038/s41467-018-06093-5.

[15] P. Zhang, Y. Wang, J. Lian, Q. Shen, C. Wang, B. Ma, Y. Zhang, T. Xu, J. Li, Y. Shao, F. Xu, J.-J. Zhu, P. Zhang, J. Lian, B. Ma, Y. Shao, F. Xu, Y. Wang, Q. Shen, C. Wang, Y. Zhang, T. Xu, J. Li, J. Zhu, Engineering the surface of smart nanocarriers using a pH-/thermal-/GSH-responsive polymer zipper for precise tumor targeting therapy in vivo, Adv. Mater. 29 (2017) 1702311, https://doi.org/10.1002/ADMA.201702311.

[16] M. Koleoso, X. Feng, Y. Xue, Q. Li, T. Munshi, X. Chen, Micro/nanoscale magnetic robots for biomedical applications, Mater. Today Bio 8 (2020) 100085, https://doi.org/10.1016/J.MTBIO.2020.100085.

[17] K. Hayashi, M. Nakamura, H. Miki, S. Ozaki, M. Abe, T. Matsumoto, W. Sakamoto, T. Yogo, K. Ishimura, Magnetically responsive smart nanoparticles for cancer treatment with a combination of magnetic hyperthermia and remote-control drug release, Theranostics 4 (2014) 834, https://doi.org/10.7150/THNO.9199.

[18] R. Ge, C. Liu, X. Zhang, W. Wang, B. Li, J. Liu, Y. Liu, H. Sun, D. Zhang, Y. Hou, H. Zhang, B. Yang, Photothermal-activatable Fe3O4 superparticle nanodrug carriers with PD-L1 immune checkpoint blockade for anti-metastatic cancer immunotherapy, ACS Appl. Mater. Interfaces 10 (2018) 20342–20355, https://doi.org/10.1021/ACSAMI.8B05876.

[19] S.D. Kong, C. Choi, J. Khamwannah, S. Jin, Magnetically vectored delivery of cancer drug using remotely on-off switchable nano capsules, IEEE Trans. Magn. 49 (2013) 349–352, https://doi.org/10.1109/TMAG.2012.2223202.

[20] J.Y. Zhu, D.W. Zheng, M.K. Zhang, W.Y. Yu, W.X. Qiu, J.J. Hu, J. Feng, X.Z. Zhang, Preferential cancer cell self-recognition and tumor self-targeting by coating nanoparticles with homotypic cancer cell membranes, Nano Lett. 16 (2016) 5895–5901, https://doi.org/10.1021/ACS.NANOLETT.6b02786.

[21] H. Jeon, J. Kim, Y.M. Lee, J. Kim, H.W. Choi, J. Lee, H. Park, Y. Kang, I.S. Kim, B. H. Lee, A.S. Hoffman, W.J. Kim, Poly-paclitaxel/cyclodextrin-SPION nano-assembly for magnetically guided drug delivery system, J. Control. Release 231 (2016) 68–76, https://doi.org/10.1016/J.JCONREL.2016.01.006.

[22] Q. Wang, J. Xiao, Y. Su, J. Huang, J. Li, L. Qiu, M. Zhan, X. He, W. Yuan, Y. Li, Fabrication of thermoresponsive magnetic micelles from amphiphilic poly(phenyl isocyanide) and Fe3O4 nanoparticles for controlled drug release and synergistic thermochemotherapy, Polym. Chem. 12 (2021) 2132–2140, https://doi.org/10.1039/D1PY00022E.

[23] Z. Xu, H. Lin, J. Dai, X. Wen, X. Yu, C. Xu, G. Ruan, Protein-nanoparticle co-assembly supraparticles for drug delivery: ultrahigh drug loading and colloidal stability, and instant and complete lysosomal drug release, Int. J. Pharm. 658 (2024) 124231, https://doi.org/10.1016/J.IJPHARM.2024.124231.

[24] L. Chu, Y. Zhang, Z. Feng, J. Yang, Q. Tian, X. Yao, X. Zhao, H. Tan, Y. Chen, Synthesis and application of a series of amphipathic chitosan derivatives and the corresponding magnetic nanoparticle-embedded polymeric micelles, Carbohydr. Polym. 223 (2019) 114966, https://doi.org/10.1016/J.CARBPOL.2019.06.005.

[25] D.H. Nguyen, J.S. Lee, J.H. Choi, K.M. Park, Y. Lee, K.D. Park, Hierarchical self-assembly of magnetic nanoclusters for theranostics: tunable size, enhanced magnetic resonance imagability, and controlled and targeted drug delivery, Acta Biomater. 35 (2016) 109–117, https://doi.org/10.1016/J.ACTBIO.2016.02.020.

[26] L. Mohammed, D. Ragab, S. Lin, S. Said, H. Gomaa, K. Mequanint, Preparation and characterization of glycol chitosan-Fe3O4 core-shell magnetic nanoparticles for controlled delivery of progesterone, J Biomater Tissue Eng 7 (2017) 561–570, https://doi.org/10.1166/JBT.2017.1603.

[27] S. Zhou, Y. Li, F. Cui, M. Jia, X. Yang, Y. Wang, L. Xie, Q. Zhang, Z. Hou, Development of multifunctional folate-poly(ethylene glycol)-chitosan-coated Fe3O4 nanoparticles for biomedical applications, Macromol. Res. 22 (2013) 58–66, https://doi.org/10.1007/S13233-014-2008-Y.

[28] L. Yan, L. Chen, X. Zhao, X. Yan, pH switchable nanoplatform for in vivo persistent luminescence imaging and precise photothermal therapy of bacterial infection, Adv. Funct. Mater. 30 (2020) 1909042, https://doi.org/10.1002/adfm.201909042.

[29] J. Park, K. An, Y. Hwang, J.E.G. Park, H.J. Noh, J.Y. Kim, J.H. Park, N.M. Hwang, T. Hyeon, Ultra-large-scale syntheses of monodisperse nanocrystals, Nat. Mater. 3 (2004) 891–895, https://doi.org/10.1038/nmat1251.

[30] J.C.F. Karnopp, J. Jorge, J.R. da Silva, D. Boldo, K.F. Del Pino Santos, A.P. Duarte, G.R. de Castro, R.B. de Azevedo, A.L. Prada, J.R.R. Amado, M.A.U. Martines, Synthesis, characterization, and cytotoxicity evaluation of Chlorambucil-functionalized mesoporous silica nanoparticles, Pharmaceutics 16 (2024) 1086, https://doi.org/10.3390/PHARMACEUTICS16081086.

[31] B. Yadav, K. Wennerberg, T. Aittokallio, J. Tang, Searching for drug synergy in complex dose-response landscapes using an interaction potency model, Comput. Struct. Biotechnol. J. 13 (2015) 504–513, https://doi.org/10.1016/j.csbj.2015.09.001.

[32] JC. Bradley, C. Neylon, R. Guha, et al., Open notebook science challenge: Solubilities of organic compounds in organic solvents, Nat Prec (2010), https://doi.org/10.1038/npre.2010.4243.2.

[33] Y. Yang, X. Zhang, C. Yu, X. Hao, J. Jie, M. Zhou, X. Zhang, Smart nanorods for highly effective cancer theranostic applications, Adv. Healthc. Mater. 3 (2014) 906–915, https://doi.org/10.1002/ADHM.201300463.

[34] D.A. Weitz, Packing in the spheres, Science 303 (2004) (1979) 968–969, https://doi.org/10.1126/SCIENCE.1094581.

[35] H. Park, K. Park, D. Kim, Preparation and swelling behavior of chitosan-based superporous hydrogels for gastric retention application, J. Biomed. Mater. Res. A 76A (2006) 144–150, https://doi.org/10.1002/JBM.A.30533.

[36] X. Feng, Y. Xue, S. Gonca, K. Ji, M. Zhang, F.R. García-García, Q. Li, Y. Huang, K. V. Kamenev, X. Chen, Ultrasmall superparamagnetic iron oxide nanoparticles for enhanced tumor penetration, J. Mater. Chem. B 11 (2023) 3422–3433, https://doi.org/10.1039/D2TB02630A.

[37] M. Yu, J. Zheng, Clearance pathways and tumor targeting of imaging nanoparticles, ACS Nano 9 (2015) 6655–6674, https://doi.org/10.1021/ACSNANO.5B01320.

[38] H. Wang, J. Feng, G. Liu, B. Chen, Y. Jiang, Q. Xie, In vitro and in vivo anti-tumor efficacy of 10-hydroxycamptothecin polymorphic nanoparticle dispersions: shape- and polymorph-dependent cytotoxicity and delivery of 10-hydroxycamptothecin to cancer cells, Nanomedicine 12 (2016) 881–891, https://doi.org/10.1016/J.NANO.2015.12.373.

[39] X. Sun, P.D. Kaufman, Ki-67: more than a proliferation marker, Chromosoma 127 (2018) 175, https://doi.org/10.1007/S00412-018-0659-8.

[40] M. Zhang, X. Chen, C. Li, X. Shen, Charge-reversal nanocarriers: an emerging paradigm for smart cancer nanomedicine, J. Control. Release 319 (2020) 46–62, https://doi.org/10.1016/J.JCONREL.2019.12.024.

[41] C. Wang, R. Zhang, J. He, L. Yu, X. Li, J. Zhang, S. Li, C. Zhang, J.C. Kagan, J. M. Karp, R. Kuai, Ultrasound-responsive low-dose doxorubicin liposomes trigger mitochondrial DNA release and activate cGAS-STING-mediated antitumour immunity, Nat. Commun. 14 (2023) 1–16, https://doi.org/10.1038/s41467-023-39607-x.

[42] S. Zanganeh, G. Hutter, R. Spitler, O. Lenkov, M. Mahmoudi, A. Shaw, J. S. Pajarinen, H. Nejadnik, S. Goodman, M. Moseley, L.M. Coussens, H.E. Daldrup-Link, Iron oxide nanoparticles inhibit tumour growth by inducing pro-inflammatory macrophage polarization in tumour tissues, Nat. Nanotechnol. 11 (2016) 986–994, https://doi.org/10.1038/nnano.2016.168.

[43] H. Raskov, A. Orhan, J.P. Christensen, I. Gögenur, Cytotoxic CD8+ T cells in cancer and cancer immunotherapy, Br. J. Cancer 124 (2020) 359–367, https://doi.org/10.1038/s41416-020-01048-4.

[44] R.Y. Ma, A. Black, B.Z. Qian, Macrophage diversity in cancer revisited in the era of single-cell omics, Trends Immunol. 43 (2022) 546–563, https://doi.org/10.1016/J.IT.2022.04.008.

[45] L. Cassetta, J.W. Pollard, A timeline of tumour-associated macrophage biology, Nat. Rev. Cancer 23 (2023) 238–257, https://doi.org/10.1038/s41568-022-00547-1.
[46] X.F. Li, C. Selli, H.L. Zhou, J. Cao, S. Wu, R.Y. Ma, Y. Lu, C. Bin Zhang, B. Xun, A. D. Lam, X.C. Pang, A. Fernando, Z. Zhang, A. Unciti-Broceta, N.O. Carragher, P. Ramachandran, N.C. Henderson, L.L. Sun, H.Y. Hu, G.B. Li, C. Sawyers, B. Z. Qian, Macrophages promote anti-androgen resistance in prostate cancer bone disease, J. Exp. Med. 220 (2023), https://doi.org/10.1084/JEM.20221007/213858.
[47] G. Solinas, G. Germano, A. Mantovani, P. Allavena, Tumor-associated macrophages (TAM) as major players of the cancer-related inflammation, J. Leukoc. Biol. 86 (2009) 1065–1073, https://doi.org/10.1189/JLB.0609385.